



Ternary Fe₃O₄@C@PANi nanocomposites as high-performance supercapacitor electrode materials

Zenghui Qiu^{1,2}, Yi Peng², Dawei He¹, Yongsheng Wang^{1,*}, and Shaowei Chen^{2,*}

¹Key Laboratory of Luminescence and Optical Information, Ministry of Education, Institute of Optoelectronic Technology, Beijing Jiaotong University, 3 Shang Yuan Cun, Hai Dian District, Beijing 100044, People's Republic of China

²Department of Chemistry and Biochemistry, University of California, 1156 High Street, Santa Cruz, CA 95064, USA

Received: 21 February 2018

Accepted: 12 May 2018

Published online:
29 May 2018

© Springer Science+Business
Media, LLC, part of Springer
Nature 2018

ABSTRACT

Ternary nanocomposites based on Fe₃O₄@C core@shell nanoparticles encapsulated in polyaniline were synthesized by using an efficient, two-step procedure and used as supercapacitor electrode materials for the first time. The morphology of the resulting Fe₃O₄@C@PANi nanocomposites was characterized by transmission electron microscopic measurements, and further structural insights were obtained by Raman, X-ray diffraction, and X-ray photoelectron spectroscopic studies. In electrochemical measurements, the resulting Fe₃O₄@C@PANi electrode exhibited a high specific capacitance of 420 F g⁻¹ at 0.5 A g⁻¹ as well as an energy density of 32.7 Wh kg⁻¹ at the power density of 500 W kg⁻¹. Additionally, the Fe₃O₄@C@PANi electrode showed excellent long-term stability with 82% retention of the capacitance after 5000 cycles at 10 A g⁻¹. These results suggest that Fe₃O₄@C@PANi-based supercapacitors may serve as high-rate energy storage systems.

Introduction

In recent years, with the rapid development of portable electronic devices and electrical vehicles, rational design and development of safe and advanced energy storage devices with high power and energy densities have been attracting extensive interest in both fundamental and technological research [1, 2]. Among these, electrochemical capacitors, or so-called supercapacitors, represent a unique technology due to their long lifetime (10⁴ cycles), wide range of working temperature, rapid charge–discharge performance, high power density (from 10 to

10⁴ W kg⁻¹), and excellent rate stability [3–8]. These significant advantages make supercapacitors promising energy storage devices for diverse applications since they can fill the gap between batteries and traditional dielectric capacitors [9–14]. However, despite a high power density (P), the energy density (E) of supercapacitors is generally low (from 0.2 to 10 Wh kg⁻¹), which hampers their practical applications [15–21]. The energy density can be enhanced by increasing the specific capacitance (C) and/or the operating potential window (V) as $E = \frac{1}{2}CV^2$. This is directly related to the choice of the electrode material, which dictates the energy storage mechanism, as

Address correspondence to E-mail: yshwang@bjtu.edu.cn; shaowei@ucsc.edu

supercapacitors can be classified into two categories: electrical double-layer capacitor (EDLC), and pseudocapacitor [22–28]. In general, the energy density of carbon-based EDLCs is much lower than that of conventional batteries. To achieve a better electrochemical performance, increasing research efforts have been devoted to advanced pseudocapacitors.

Binary composites based on transition metal oxides/hydroxides and conducting polymers have been widely used as pseudocapacitor electrode materials owing to their relatively low costs, ease of preparation, high theoretical specific capacity, and electrochemical reversibility [29–32]. Yet, their low conductivity and unsatisfactory durability significantly limit their practical applications [31, 33, 34]. To mitigate these issues, substantial efforts have been devoted to the rational design and engineering of ternary composites, in particular, hybrids of carbonaceous materials, transition metal oxides, and conducting polymers, as a new promising candidate of electrode materials [29, 31, 35–38]. Of these, activated carbon is an ideal carbonaceous material due to excellent electrical conductivity, good mechanical strength, and chemical inertness [39–41]. Of the metal oxides/hydroxides, Fe_3O_4 represents a viable structural component owing to its good redox activities, environmentally friendly nature, large operational potential window (−1.2 to +0.25 V), high theoretical capacity (2299 F g^{-1}), natural abundance, and low costs [42–46]. For the conducting polymers, polyaniline (PANi) is a popular choice, because of its low costs, ease of synthesis, high theoretical specific pseudocapacitance, high doping–dedoping rate during the charge–discharge process, and high electrical conductivity [47–49]. Note that PANi can store charges at the electrical double layer as well by faradaic charge transfer. Moreover, like other transition metal oxides, the low electrical conductivity of Fe_3O_4 results in compromises of power density. To address this issue, our work focuses on incorporation of Fe_3O_4 into electrically conductive frameworks, such as PANi, forming Fe_3O_4 conductive framework hybrid nanostructures. Indeed, ternary composites by the combination of PANi with activated carbon and transition metal oxides have been recognized as a high electrochemical properties material for enhanced energy storage capacity [50, 51]. Owing to the synergistic effect of the different components in the ternary composites, the electrode not only provides high electrical conductivity and remarkable

cycling stability, but also increases the specific capacitance and energy density of the overall structure.

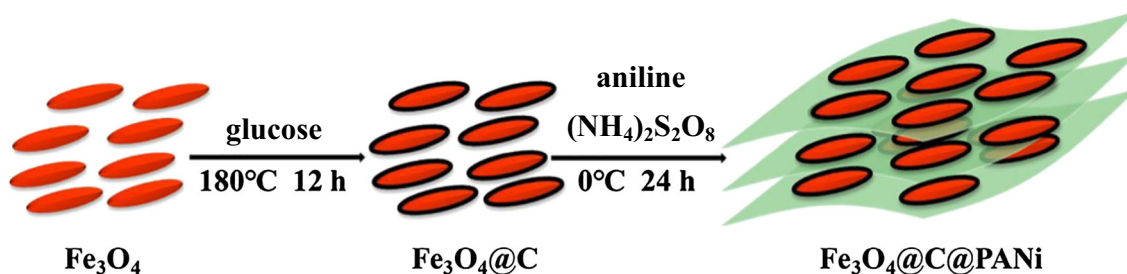
Herein, ternary nanocomposites based on $\text{Fe}_3\text{O}_4@\text{C}$ core@shell nanoparticles encapsulated in PANi were prepared by a facile two-step synthetic method and used as electrode materials for high-performance supercapacitors for the first time. The advanced $\text{Fe}_3\text{O}_4@\text{C}@PANi$ supercapacitor device exhibited excellent electrochemical properties, such as a high specific capacitance of 420 F g^{-1} at 0.5 A g^{-1} , 160 F g^{-1} at 50 A g^{-1} , an energy density of 32.7 Wh kg^{-1} (at the power density of 500 W kg^{-1}), and good long-term stability (82% capacitance retention after 5000 cycles). The results suggest a new strategy in the design and fabrication of ternary nanocomposites for high-performance energy storage applications.

Experimental section

Synthesis of ternary $\text{Fe}_3\text{O}_4@\text{C}@PANi$ nanocomposites

$\text{Fe}_3\text{O}_4@\text{C}$ core@shell nanocomposites were synthesized by a hydrothermal strategy (Scheme 1) [2]. Briefly, 0.6 g of glucose was dissolved into a solution containing 150 mL of deionized water, 1.2 g of $\text{FeCl}_3 \cdot 6\text{H}_2\text{O}$, 3.6 g of sodium acetate, and 30 mL of ethylene diamine. The solution was then transferred into a 200 mL Teflon-lined autoclave and heated at $180 \text{ }^\circ\text{C}$ for 12 h. The products were cooled down naturally, separated by filtration, washed for several times with water, and finally collected by centrifugation. The obtained sample was then dried in oven at $60 \text{ }^\circ\text{C}$ for 12 h, affording $\text{Fe}_3\text{O}_4@\text{C}$ core@shell nanocomposites. As a comparison, pure Fe_3O_4 was also synthesized in the same manner but without the addition of glucose.

Ternary $\text{Fe}_3\text{O}_4@\text{C}@PANi$ nanocomposites were prepared by adopting a polymerization method [38], as illustrated in Scheme 1. Briefly, 1.8 g of the $\text{Fe}_3\text{O}_4@\text{C}$ prepared above was dispersed into 160 mL of H_2SO_4 (0.5 M) under sonication. 0.6 mL of aniline monomer was then added into the solution under vigorous magnetic stirring at $0 \text{ }^\circ\text{C}$ for 1 h, into which was then added in a dropwise fashion 40 mL of H_2SO_4 (0.5 M) containing 1.5 g of $(\text{NH}_4)_2\text{S}_2\text{O}_8$. The obtained solution was placed in an ice bath ($\sim 5 \text{ }^\circ\text{C}$)



Scheme 1 Schematic illustration of the synthetic process of the ternary $\text{Fe}_3\text{O}_4@\text{C}@\text{PANi}$ nanocomposites.

under mechanical stirring for 24 h to allow the polymerization process to complete. The final products were collected by centrifugation, rinsed with ethanol and deionized water to remove the impurities, and dried at 60 °C for 24 h.

Characterization

The morphologies of Fe_3O_4 , $\text{Fe}_3\text{O}_4@\text{C}$ and $\text{Fe}_3\text{O}_4@\text{C}@\text{PANi}$ were characterized by field-emission scanning electron microscopy (FESEM, Quant 250FEG) and transmission electron microscopy (TEM, JEOL JEM-2010F) measurements. Elemental mapping studies based on energy dispersive X-ray (EDX) analysis and selected-area electron diffraction (SAED) were carried out on the JEOL 2010F microscope. The crystal structures of the samples were investigated by powder X-ray diffraction (XRD) measurements on a BRUKER diffractometer (D8 advance CuK_α radiation source, $\lambda = 0.15406$ nm), and Raman spectra were acquired with a Renishaw in Via micro-Raman system (Thermo Fischer DXR) with a He–Ne laser beam at the excitation wavelength of 532 nm under ambient conditions. X-ray photoelectron spectroscopy (XPS) tests were performed using a Kratos-Axis spectrometer with a monochromatic Al K_α (1486.6 eV) X-ray source (15 kV and 10 mA) and a hemispherical electron energy analyzer.

Electrochemistry

A two-electrode cell system was employed to measure the electrochemical performance of the as-prepared electrodes in 1 M KOH electrolyte with a porous nonwoven cloth separator. The working electrodes were prepared by pressing a homogeneous slurry containing 80 wt% $\text{Fe}_3\text{O}_4@\text{C}$ or $\text{Fe}_3\text{O}_4@\text{C}@\text{PANi}$ as the active materials, 10 wt% carbon black, and 10 wt% polytetrafluoroethylene (PTFE) with a small amount of ethanol onto a nickel

foam current collector (1 cm × 1 cm, under a pressure of 10 MPa). The mass of the active materials ($\text{Fe}_3\text{O}_4@\text{C}$ or $\text{Fe}_3\text{O}_4@\text{C}@\text{PANi}$) for all electrodes was controlled to be about 1.5 mg. After being dried at 90 °C for 12 h in a vacuum oven, the working electrodes were immersed in 1 M KOH aqueous solution for 24 h to ensure equilibrium contact between the active materials and electrolyte. All electrochemical measurements including cyclic voltammetry (CV), galvanostatic charge–discharge (GCD), and electrochemical impedance spectroscopy (EIS) were carried out at ambient temperature with a CHI 660B electrochemical workstation.

Results and discussion

Morphology and structure characteristics

The morphologic structures of the as-prepared samples were firstly characterized by TEM measurements. From Fig. 1a, one can see that the Fe_3O_4 nanoparticles exhibited a spindle-like shape, of ca. 100 nm in length and ca. 10 nm in cross-sectional diameter. For the $\text{Fe}_3\text{O}_4@\text{C}$ sample (Fig. 1b), it can be clearly observed that the Fe_3O_4 surface was uniformly covered by an activated carbon film. For the $\text{Fe}_3\text{O}_4@\text{C}@\text{PANi}$ nanocomposites (Fig. 1c), the $\text{Fe}_3\text{O}_4@\text{C}$ can be seen to be encapsulated with a PANi film and formed aggregates of 100–200 nm across. (This is also manifested in FESEM measurements, Fig. 1c inset.) In HRTEM and SAED studies (Fig. 1d), the Fe_3O_4 nanoparticles can be seen to display well-defined lattice fringes with an interplanar spacing of around 0.253 nm, consistent with that of the Fe_3O_4 (311) crystalline planes [52]. The SAED patterns (Fig. 1d inset) are also in good agreement with those of Fe_3O_4 [52].

Further structural insights were obtained by EDX studies (Fig. 2a), where the elements of C, O, Fe, and

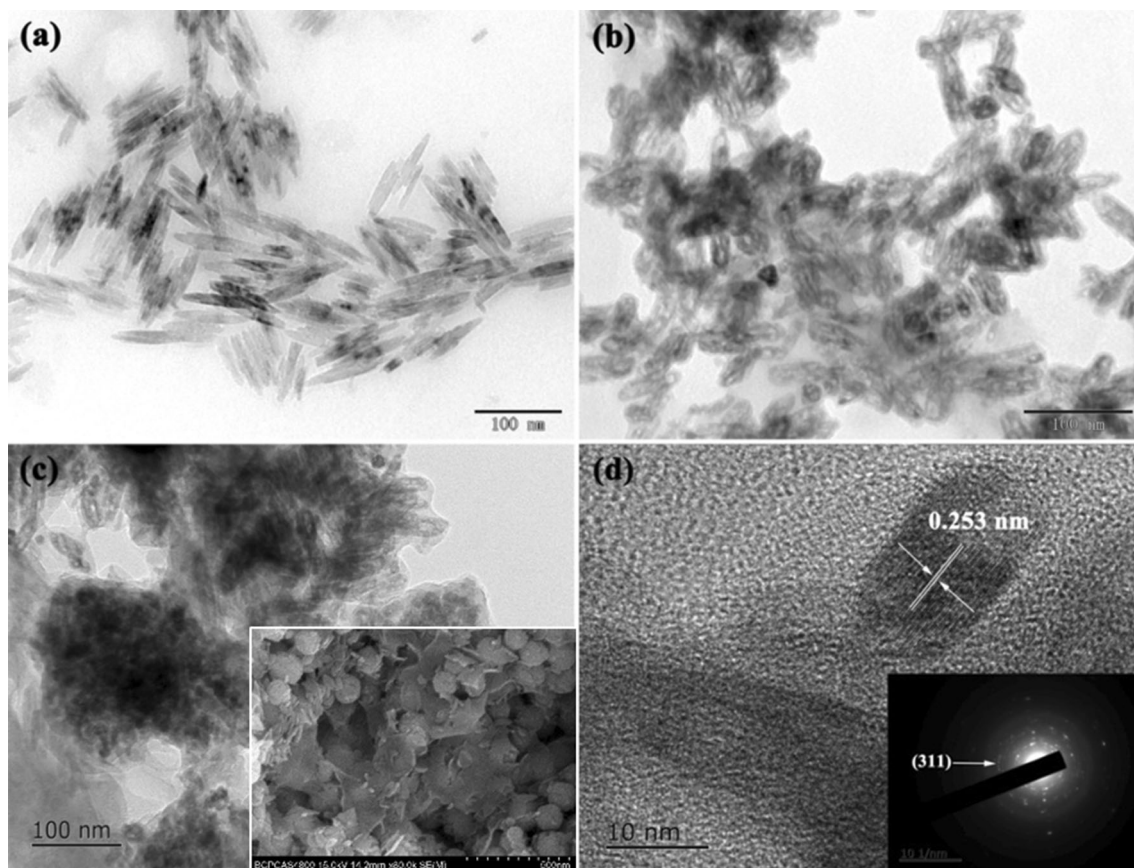


Figure 1 Representative TEM images of **a** Fe_3O_4 , **b** $\text{Fe}_3\text{O}_4@\text{C}$, and **c** $\text{Fe}_3\text{O}_4@\text{C}@\text{PANi}$. Scale bars are all 100 nm. Inset to panel (c) is a corresponding SEM image, with a scale bar of 500 nm.

N can be readily identified in the sample (Fig. 2b). From the corresponding elemental maps (Fig. 2c–f), these elements can be seen to be rather evenly distributed within the nanocomposites, further confirming the formation of ternary nanocomposites.

From the Raman spectra in Fig. 3a, one can see that both $\text{Fe}_3\text{O}_4@\text{C}$ (red curve) and $\text{Fe}_3\text{O}_4@\text{C}@\text{PANi}$ (green curve) exhibited a pair of prominent peaks. The one centered at 1355 cm^{-1} is the so-called D band corresponding to edges and/or defective sites of graphitic carbon, and the other at 1595 cm^{-1} is defined as the G band, corresponding to the vibration of sp^2 -hybridized carbon. These are very well defined with carbon black (black curve). Additionally, we have calculated the I_D/I_G values for the D and G bands of the samples in Raman spectra: 1.03 for carbon black (black curve), 1.04 for $\text{Fe}_3\text{O}_4@\text{C}$ (red curve), and 1.05 for $\text{Fe}_3\text{O}_4@\text{C}@\text{PANi}$ (green curve). Two additional peaks can also be seen at 1160 and 1490 cm^{-1} with the $\text{Fe}_3\text{O}_4@\text{C}@\text{PANi}$ nanocomposites,

d Representative HRTEM image of Fe_3O_4 , with a scale bar of 10 nm. Inset is the corresponding SAED patterns.

due to C–H vibrations of the benzenoid ring and C–N stretching deformation of the quinonoid units in PANi. The XRD patterns of the samples are shown in Fig. 3b. In all the curves (carbon, $\text{Fe}_3\text{O}_4@\text{C}$ and $\text{Fe}_3\text{O}_4@\text{C}@\text{PANi}$), the strong peak at 26° is due to the C (002) diffraction. The XRD patterns of $\text{Fe}_3\text{O}_4@\text{C}$ composites exhibited peaks centered at 21° , 35.7° , 43.3° , 53.7° , 62.5° , and 67° , corresponding to the (220), (311), (400), (422), (333), and (440) diffractions of Fe_3O_4 , respectively [53, 54]. These peaks can be clearly found in $\text{Fe}_3\text{O}_4@\text{C}@\text{PANi}$ nanocomposites as well. Furthermore, no well-defined diffraction patterns can be identified for PANi, suggesting its amorphous nature [55].

To further reveal the chemical composition and bonding nature of the various elements in the nanocomposites, XPS measurements were carried out and the results are shown in Fig. 4. From the survey spectrum in Fig. 4a, four peaks can be identified for $\text{Fe}_3\text{O}_4@\text{C}@\text{PANi}$ at around 285, 400, 532, and 712 eV,

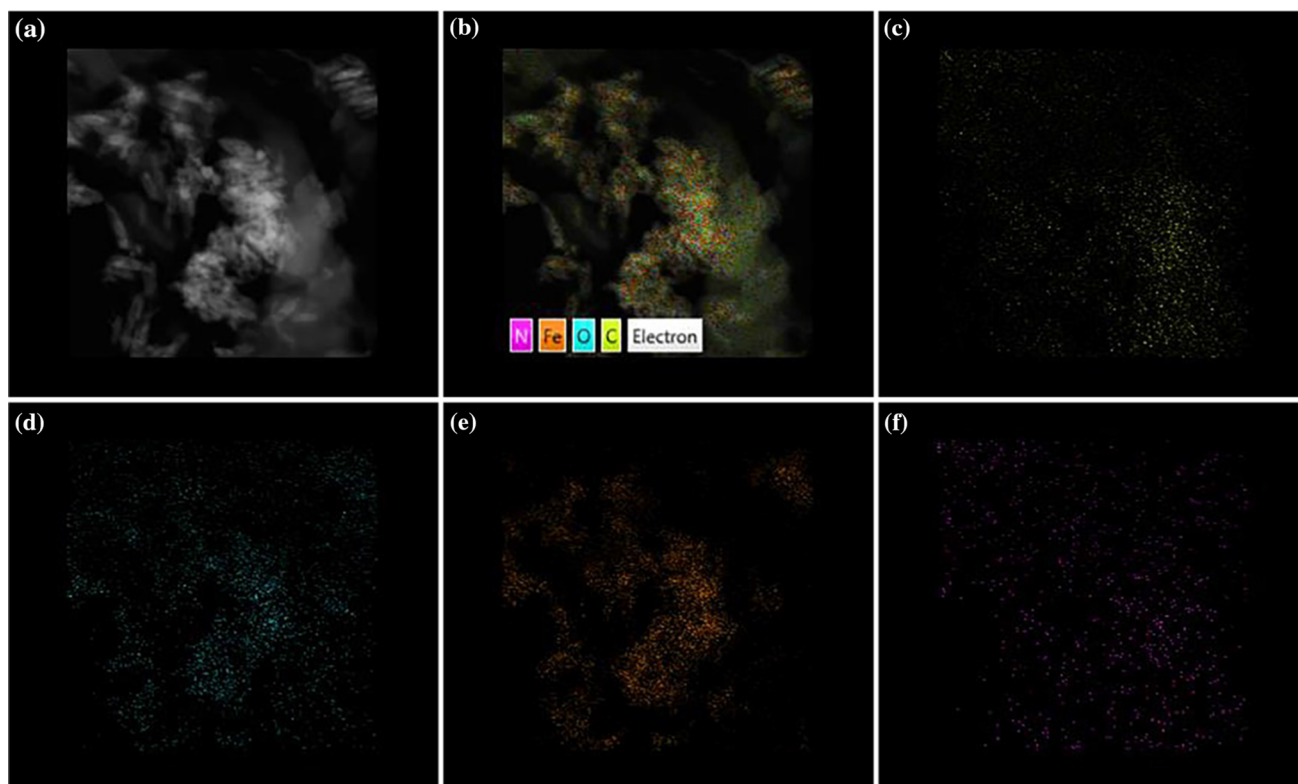


Figure 2 a, b EDX patterns of $\text{Fe}_3\text{O}_4@\text{C}@\text{PANI}$, with the corresponding elemental maps of c C, d O, e Fe, and f N in the $\text{Fe}_3\text{O}_4@\text{C}@\text{PANI}$ nanocomposites.

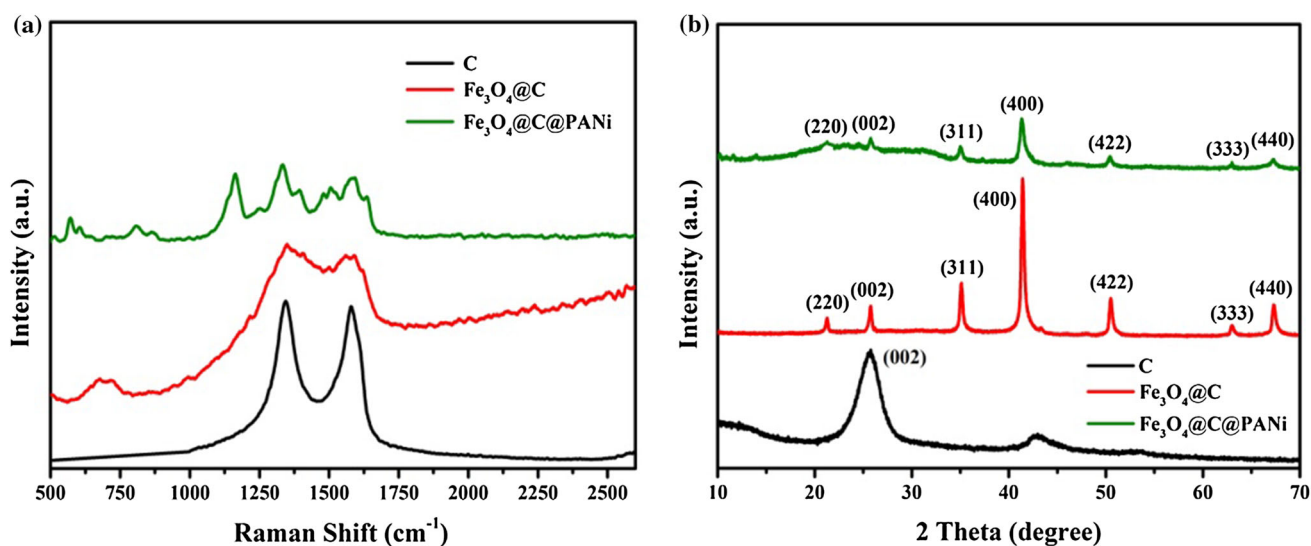


Figure 3 a Raman spectra and b XRD patterns of C, $\text{Fe}_3\text{O}_4@\text{C}$, and $\text{Fe}_3\text{O}_4@\text{C}@\text{PANI}$.

which may be assigned to the C 1s, N1s, O 1s, and Fe 2p electrons, respectively [56]. The formation of PANi can be seen by high-resolution scans of the C1 s electrons, where deconvolution of the spectrum yielded three peaks at 284.8, 285.6, and 288.9 eV, due

to C–C/C=C, C–O/C–N, and C=O, respectively (Fig. 4b) [52]. In Fig. 4c, the high-resolution scan of N1 s electrons was deconvoluted into three peaks at 399.3, 400.1, and 401.8 eV, which correspond to imine (=N–), amine (–NH–), and protonated amine (–N⁺–),

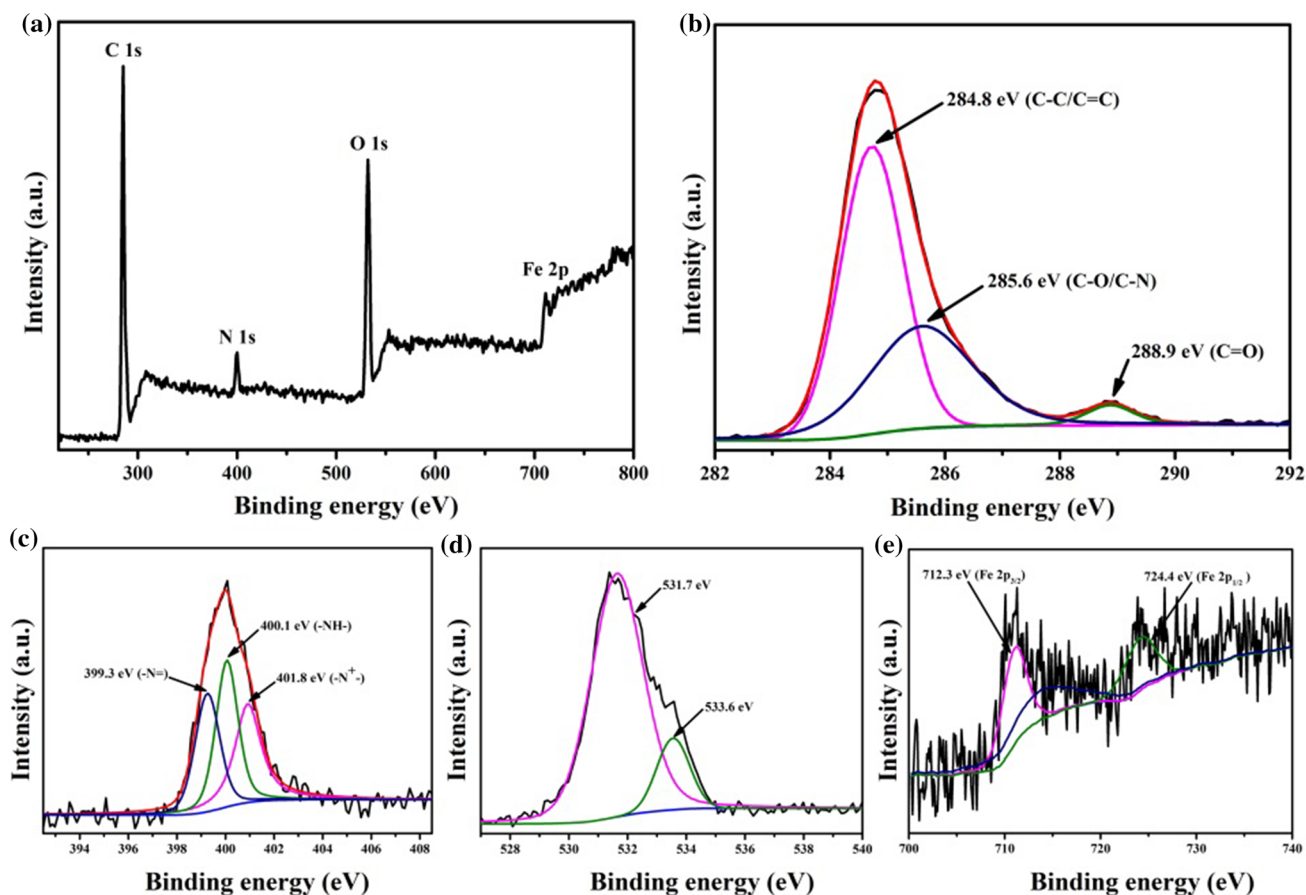


Figure 4 a XPS survey spectrum and high-resolution scans of **b** C 1s, **c** N 1s, **d** O 1s, and **e** Fe 2p electrons of $\text{Fe}_3\text{O}_4@\text{C}@\text{PANI}$.

respectively [57]. In the O1s spectrum (Fig. 4d), two peaks were resolved at 531.7 and 533.6 eV, due to oxygen bonded to Fe and C, respectively. Figure 4e displays the Fe 2p spectrum, and the peaks centered at 712.3 and 724.4 eV were consistent with the Fe $2p_{3/2}$ and Fe $2p_{1/2}$ electrons of Fe_3O_4 , respectively [58]. Additionally, based on the integrated peak areas, the elemental composition in $\text{Fe}_3\text{O}_4@\text{C}@\text{PANI}$ nanocomposites can be estimated to be 68.3 at.% for C, 10.2 at.% for N, 17.2 at.% for O, and 4.3 at.% for Fe.

Electrochemical characterizations

Capacitance characteristics of these nanocomposites were then examined by CV, GCD, and EIS measurements within the potential range of 0 to + 0.7 V. Figure 5a shows the CV curves of the $\text{Fe}_3\text{O}_4@\text{C}$ and $\text{Fe}_3\text{O}_4@\text{C}@\text{PANI}$ electrodes at the potential scan rate of 50 mV s^{-1} in a 1 M KOH electrolyte. It can be clearly observed that all CV curves are quasi-rectangular in shape without any obvious redox peaks, and

the CV curve of the $\text{Fe}_3\text{O}_4@\text{C}@\text{PANI}$ electrode shows a larger integration area than that of the $\text{Fe}_3\text{O}_4@\text{C}$ electrode, indicating a better capacitive performance and faster charge/discharge property for power storage of the former.

To further evaluate the charge storage properties of these electrodes, we also measured GCD curves at the same current density of 1 A g^{-1} (Fig. 5b). It can be seen that the $\text{Fe}_3\text{O}_4@\text{C}@\text{PANI}$ electrode exhibited a longer discharge time, and the specific capacitance (380 F g^{-1}) was indeed higher than that (120 F g^{-1}) of the $\text{Fe}_3\text{O}_4@\text{C}$ electrode. This suggests enhanced charge storage property with the encapsulation of $\text{Fe}_3\text{O}_4@\text{C}$ by a conducting polymer film of PANi, in good agreement with the CV results. Additionally, the GCD curves of both $\text{Fe}_3\text{O}_4@\text{C}$ and $\text{Fe}_3\text{O}_4@\text{C}@\text{PANI}$ display a quasi-triangular shape, signifying the combined contributions of both double-layer capacitance from C and pseudocapacitance from PANi chains as well as Fe_3O_4 nanoparticles (though

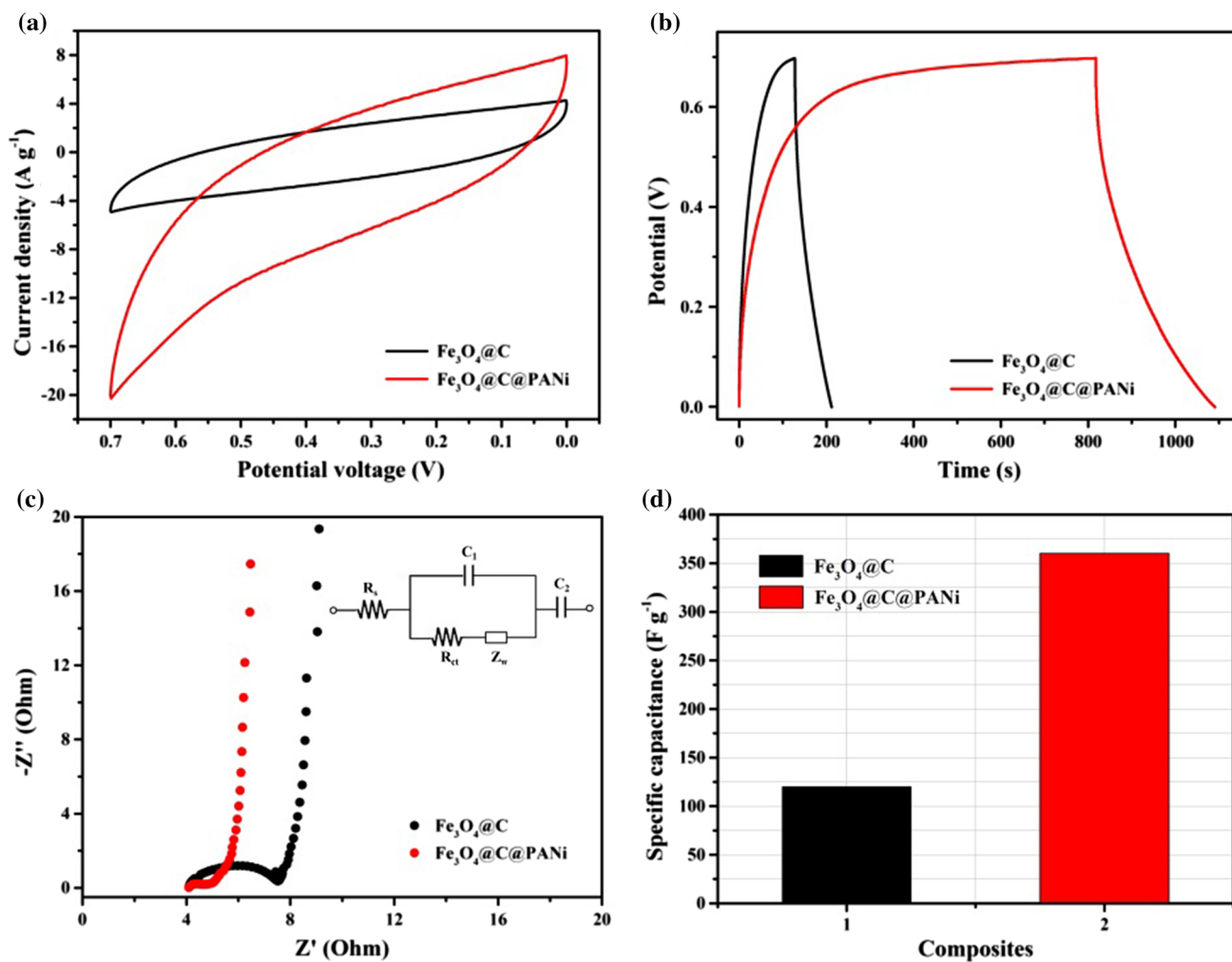


Figure 5 **a** CV curves of $\text{Fe}_3\text{O}_4@\text{C}$ and $\text{Fe}_3\text{O}_4@\text{C}@\text{PANi}$ at the potential scan rate of 50 mV s^{-1} . **b** GCD curves of $\text{Fe}_3\text{O}_4@\text{C}$ and $\text{Fe}_3\text{O}_4@\text{C}@\text{PANi}$ at the current density of 1 A g^{-1} . **c** Nyquist

impedance plots of $\text{Fe}_3\text{O}_4@\text{C}$ and $\text{Fe}_3\text{O}_4@\text{C}@\text{PANi}$ at 0 V , with the equivalent circuit shown in the inset. **d** the corresponding specific capacitance.

no well-defined voltammetric peaks are seen in Fig. 5a).

To evaluate the electrical conductivity of the nanocomposites, EIS tests were carried out in the range of 0.1 Hz – 100 kHz . Figure 5c depicts the Nyquist plots, and the equivalent circuit is shown in the inset, where the semicircle in the high-frequency region reflects the interfacial charge-transfer resistance (R_{ct}) and the linear part in the low-frequency region refers to the Warburg resistance (W_d) due to diffusion of electrolyte species [59]. It can be seen that whereas the shape of the semicircle is similar for both $\text{Fe}_3\text{O}_4@\text{C}$ and $\text{Fe}_3\text{O}_4@\text{C}@\text{PANi}$, R_{ct} is significantly smaller for $\text{Fe}_3\text{O}_4@\text{C}@\text{PANi}$ (1.5Ω) than for $\text{Fe}_3\text{O}_4@\text{C}$ (3.8Ω), indicative of enhanced electron-transfer kinetics. In addition, the intercept (R_s) to the x -axis

can be estimated to be 3.8Ω for $\text{Fe}_3\text{O}_4@\text{C}$ and 1.55Ω for $\text{Fe}_3\text{O}_4@\text{C}@\text{PANi}$, signifying that indeed the incorporation of a PANi layer enhanced the electrical conductivity of the nanocomposites. Notably, one can see that the slope of the linear segments greater for $\text{Fe}_3\text{O}_4@\text{C}@\text{PANi}$ than for $\text{Fe}_3\text{O}_4@\text{C}$, indicating increasingly capacitive nature of the former. Furthermore, from GCD curves (Fig. 5b), the specific capacitance was estimated to be 120 F g^{-1} for $\text{Fe}_3\text{O}_4@\text{C}$ and almost tripled to 380 F g^{-1} for $\text{Fe}_3\text{O}_4@\text{C}@\text{PANi}$ at 1 A g^{-1} , as shown in Fig. 5d.

With such a remarkable performance, the $\text{Fe}_3\text{O}_4@\text{C}@\text{PANi}$ nanocomposites were then used to construct a symmetric supercapacitor (Fig. 6a). Figure 6b displays the CV curves of the supercapacitor at various scan rates from 20 to 200 mV s^{-1} . All the curves

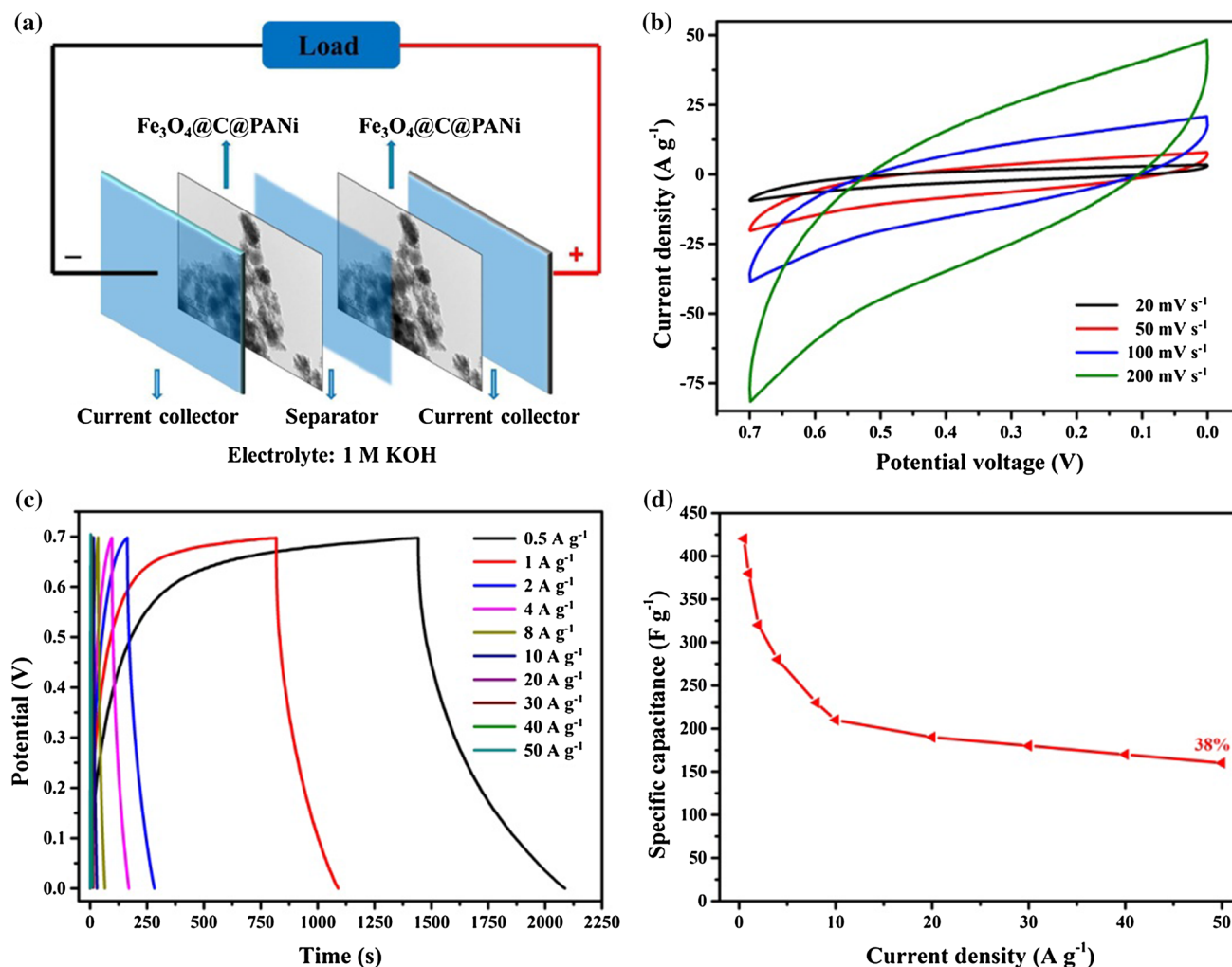


Figure 6 a Schematic diagram of a symmetric $\text{Fe}_3\text{O}_4@\text{C}@\text{PANi}$ supercapacitor device. b CV curves of the device at different scan rates. c GCD curves of the device at various current densities and d specific capacitance versus current density plot of $\text{Fe}_3\text{O}_4@\text{C}@\text{PANi}$.

exhibit a nearly rectangular-like shape without obvious redox peaks even at an ultrahigh scan rate, indicating ideal capacitive behavior and good rate capability of our device. As shown in Fig. 6c, there is no clear IR drop in GCD measurements within the current density range of 0.5–50 A g^{-1} , indicating facile electron transfer and electrolyte ion diffusion in the device. Additionally, the GCD curves were all nearly symmetric, indicative of good charge–discharge stability. The specific capacitance (C) of the electrode can be calculated from the GCD curves, $C = I\Delta t/(m\Delta V)$, where I is the specific current, Δt is the discharge time, m is the mass of the electroactive materials in the electrodes, and ΔV is the voltage range.

Figure 6d depicts the specific capacitances of $\text{Fe}_3\text{O}_4@\text{C}@\text{PANi}$ at different current densities, which

decreased with the increase in the discharge current densities. Nevertheless, $\text{Fe}_3\text{O}_4@\text{C}@\text{PANi}$ can be seen to exhibit a high specific capacitance from 420 to 160 F g^{-1} as the current densities vary from 0.5 to 50 A g^{-1} . In addition, 38% of the initial specific capacitance was retained when the discharge rate was increased from 0.5 to 50 A g^{-1} . This suggests good rate capability due to the small charge-transfer resistance.

Long-term cycle stability is another significant factor in practical applications, which was evaluated through consecutive charge–discharge process at the current density of 10 A g^{-1} for up to 5000 cycles, and the results are depicted in Fig. 7a. One can notice that more than 80% of the capacitance was retained and the shape of GCD curves did not change appreciably, suggesting a low leakage current and excellent long-

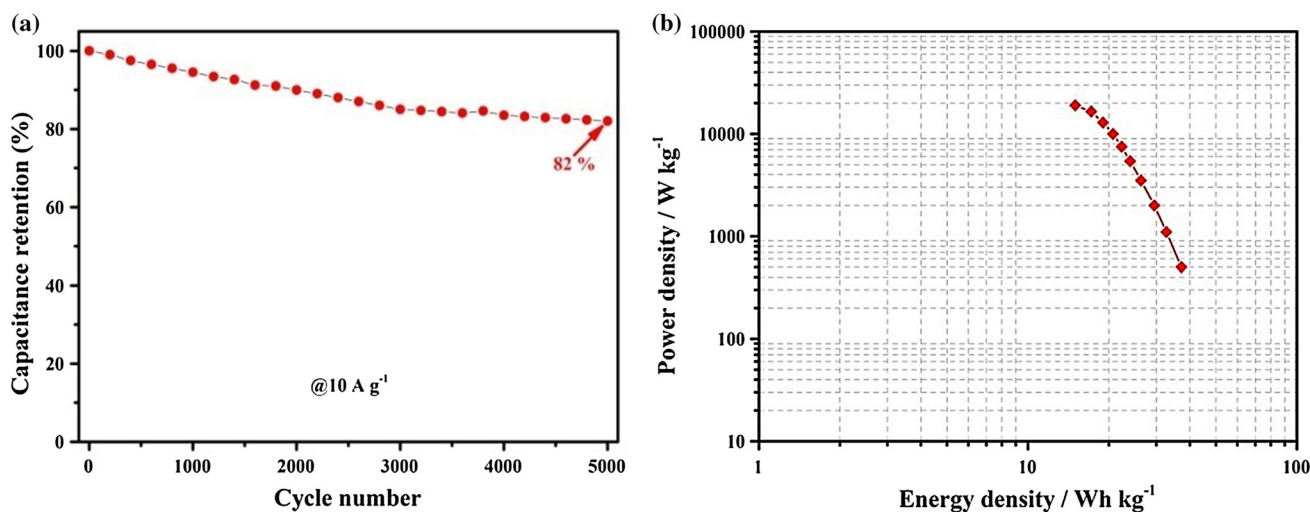


Figure 7 **a** Cycling stability of the $\text{Fe}_3\text{O}_4@\text{C}@\text{PANi}$ measured at 10 A g^{-1} for 5000 cycles. **b** The corresponding Ragone plot.

term cyclic stability of the FCP electrode materials. From the Ragone plot in Fig. 7b, one can see that the symmetric supercapacitor device displays a maximum energy density of 32.7 Wh kg^{-1} at a power density of 500 W kg^{-1} ; and even at the high power density of $19,000 \text{ W kg}^{-1}$, it still maintains an energy density of 15.5 Wh kg^{-1} . This suggests that $\text{Fe}_3\text{O}_4@\text{C}@\text{PANi}$ ternary nanocomposites may serve as effective electrode materials for high-rate electrochemical energy storage devices.

Conclusions

In summary, ternary $\text{Fe}_3\text{O}_4@\text{C}@\text{PANi}$ nanocomposites were synthesized by a multi-step strategy and the electrochemical properties were examined. The formation of a PANi overlayer facilitated electron transfer. Owing to the synergistic effects of the highly conductive carbon and PANi components and significant pseudocapacitance contributions from PANi and Fe_3O_4 particles, the sandwich-like $\text{Fe}_3\text{O}_4@\text{C}@\text{PANi}$ nanocomposites exhibited an excellent electrochemical performance as a supercapacitor electrode, with a large specific capacitance of 420 F g^{-1} at 0.5 A g^{-1} , high energy density of 32.7 Wh kg^{-1} , and good rate capability. (Thirty-eight percent retention with the current density increased by 100 times.) Overall, the results offer a new, effective strategy in the design and preparation of ternary nanocomposites for high-performance electrochemical capacitors.

Acknowledgements

This work was supported, in part, by the National Basic Research Program of China (2016YFA0202300, 2016YFA0202302), the National Natural Science Foundation of China (61527817, 61335006, 61378073), and Beijing Science and Technology Committee (Z151100003315006). S. W. C. thanks the National Science Foundation for partial support of the work under Grants CHE-1710408 and DMR-1409396.

References

- [1] Wang G, Zhang L, Zhang J (2012) A review of electrode materials for electrochemical supercapacitors. *Chem Soc Rev* 41:797–828. <https://doi.org/10.1039/c1cs15060j>
- [2] Sun D, Zou Q, Wang Y, Wang Y, Jiang W, Li F (2014) Controllable synthesis of porous $\text{Fe}_3\text{O}_4@\text{ZnO}$ sphere decorated graphene for extraordinary electromagnetic wave absorption. *Nanoscale* 6:6557–6562. <https://doi.org/10.1039/c3nr06797a>
- [3] Wu ZS, Parvez K, Feng X, Mullen K (2013) Graphene-based in-plane micro-supercapacitors with high power and energy densities. *Nat Commun* 4:2487. <https://doi.org/10.1038/ncomms3487>
- [4] Liu C, Li F, Ma L-P, Cheng H-M (2010) Advanced mater for energy storage. *Adv Mater* 22:E28–E62. <https://doi.org/10.1002/adma.200903328>
- [5] Chu S, Majumdar A (2012) Opportunities and challenges for a sustainable energy future. *Nature* 488:294–303. <https://doi.org/10.1038/nature11475>

- [6] Yan J, Fan Z, Sun W et al (2012) Advanced asymmetric supercapacitors based on Ni(OH)₂/graphene and porous graphene electrodes with high energy density. *Adv Funct Mater* 22:2632–2641. <https://doi.org/10.1002/adfm.201102839>
- [7] Yoo JJ, Balakrishnan K, Huang J et al (2011) Ultrathin planar graphene supercapacitors. *Nano Lett* 11:1423–1427. <https://doi.org/10.1021/nl200225j>
- [8] Lu XF, Chen XY, Zhou W, Tong YX, Li GR (2015) α -Fe₂O₃@PANI Core–Shell nanowire arrays as negative electrodes for asymmetric supercapacitors. *ACS Appl Mater Interfaces* 7:14843–14850. <https://doi.org/10.1021/acsami.5b03126>
- [9] Rakhi RB, Chen W, Cha D, Alshareef HN (2012) Substrate dependent self-organization of mesoporous cobalt oxide nanowires with remarkable pseudocapacitance. *Nano Lett* 12:2559–2567. <https://doi.org/10.1021/nl300779a>
- [10] Shen L, Wang J, Xu G, Li H, Dou H, Zhang X (2015) NiCo₂S₄ Nanosheets grown on nitrogen-doped carbon foams as an advanced electrode for supercapacitors. *Adv Energy Mater* 5:1400977. <https://doi.org/10.1002/aenm.201400977>
- [11] Xiong P, Zhu J, Wang X (2015) Recent advances on multi-component hybrid nanostructures for electrochemical capacitors. *J Power Sources* 294:31–50. <https://doi.org/10.1016/j.jpowsour.2015.06.062>
- [12] Acerce M, Voiry D, Chhowalla M (2015) Metallic 1T phase MoS₂ nanosheets as supercapacitor electrode materials. *Nat Nanotechnol* 10:313–318. <https://doi.org/10.1038/nnano.2015.40>
- [13] Wang AL, Xu H, Feng JX, Ding LX, Tong YX, Li GR (2013) Design of Pd/PANI/Pd sandwich-structured nanotube array catalysts with special shape effects and synergistic effects for ethanol electrooxidation. *J Am Chem Soc* 135:10703–10709. <https://doi.org/10.1021/ja403101r>
- [14] Feng JX, Ding LX, Ye SH et al (2015) Co(OH)₂ @PANI hybrid nanosheets with 3D networks as high-performance electrocatalysts for hydrogen evolution reaction. *Adv Mater* 27:7051–7057. <https://doi.org/10.1002/adma.201503187>
- [15] Senthilkumar ST, Wang Y, Huang H (2015) Advances and prospects of fiber supercapacitors. *J Mater Chem A* 3:20863–20879. <https://doi.org/10.1039/c5ta04731e>
- [16] Yang Y, Ruan G, Xiang C, Wang G, Tour JM (2014) Flexible three-dimensional nanoporous metal-based energy devices. *J Am Chem Soc* 136:6187–6190. <https://doi.org/10.1021/ja501247f>
- [17] Huang Y, Hu H, Huang Y et al (2015) From industrially weavable and knittable highly conductive yarns to large wearable energy storage textiles. *ACS Nano* 9:4766–4775. <https://doi.org/10.1021/acs.nano.5b00860>
- [18] Kumar R, Singh RK, Dubey PK, Singh DP, Yadav RM, Tiwari RS (2015) Freestanding 3D graphene–nickel encapsulated nitrogen-rich aligned bamboo like carbon nanotubes for high-performance supercapacitors with robust cycle stability. *Adv Mater Interfaces* 2:1500191. <https://doi.org/10.1002/admi.201500191>
- [19] Kumar R, Singh RK, Savu R, Dubey PK, Kumar P, Moshkalev SA (2016) Microwave-assisted synthesis of void-induced graphene-wrapped nickel oxide hybrids for supercapacitor applications. *RSC Adv* 6:26612–26620. <https://doi.org/10.1039/C6RA00426A>
- [20] Kumar R, Savu R, Joanni E, Vaz AR, Canesqui MA, Singh RK, Timm RA, Kubota LT, Moshkalev SA (2016) Fabrication of interdigitated micro-supercapacitor devices by direct laser writing onto ultra-thin, flexible and free-standing graphite oxide films. *RSC Adv* 6:84769–84776. <https://doi.org/10.1039/C6RA17516C>
- [21] Yadav SK, Kumar R, Sundramoorthy AK, Singh RK, Koo CM (2016) Simultaneous reduction and covalent grafting of polythiophene on graphene oxide sheets for excellent capacitance retention. *RSC Adv* 6:52945–52949. <https://doi.org/10.1039/c6ra07904k>
- [22] Conway BE, Pell WG (2003) Double-layer and pseudocapacitance types of electrochemical capacitors and their applications to the development of hybrid devices. *J Solid State Electrochem* 7:637–644. <https://doi.org/10.1007/s10008-003-0395-7>
- [23] Gupta RK, Candler J, Palchoudhury S, Ramasamy K, Gupta BK (2015) Flexible and high performance supercapacitors based on NiCo₂O₄ for wide temperature range applications. *Sci Rep* 5:15265. <https://doi.org/10.1038/srep15265>
- [24] Abbas SA, Jung K-D (2016) Preparation of mesoporous microspheres of NiO with high surface area and analysis on their pseudocapacitive behavior. *Electrochim Acta* 193:145–153. <https://doi.org/10.1016/j.electacta.2016.02.054>
- [25] Ye SB, Feng JC, Wu PY (2013) Deposition of three-dimensional graphene aerogel on nickel foam as a binder-free supercapacitor electrode. *ACS Appl Mater Interfaces* 5:7122–7129. <https://doi.org/10.1021/am401458x>
- [26] Kumar R, Singh RK, Vaz AR, Savu R, Moshkalev SA (2017) Self-assembled and one-step synthesis of interconnected 3D network of Fe₃O₄/reduced graphene oxide nanosheets hybrid for high-performance supercapacitor electrode. *ACS Appl Mater Interfaces* 9:8880–8890. <https://doi.org/10.1021/acsami.6b14704>
- [27] Kumar R, Singh RK, Dubey PK, Singh DP, Yadav RM, Tiwari RS (2015) Hydrothermal synthesis of a uniformly dispersed hybrid graphene–TiO₂ nanostructure for optical

- and enhanced electrochemical applications. *RSC Adv* 5:7112–7120. <https://doi.org/10.1039/c4ra06852a>
- [28] Kumar R, Singh RK, Vaz AR, Moshkalev SA (2015) Microwave-assisted synthesis and deposition of a thin ZnO layer on microwave-exfoliated graphene: optical and electrochemical evaluations. *RSC Adv* 5:67988–67995. <https://doi.org/10.1039/c5ra09936f>
- [29] Wang B, Zhu T, Wu HB, Xu R, Chen JS, Lou XW (2012) Porous Co_3O_4 nanowires derived from long $\text{Co}(\text{CO}_3)_0.5(\text{OH})\cdot 0.11\text{H}_2\text{O}$ nanowires with improved supercapacitive properties. *Nanoscale* 4:2145–2149. <https://doi.org/10.1039/c2nr11897a>
- [30] Cai G, Darmawan P, Cui M et al (2016) Highly stable transparent conductive silver grid/PEDOT:PSS electrodes for integrated bifunctional flexible electrochromic supercapacitors. *Adv Energy Mater* 6:1501882. <https://doi.org/10.1002/aenm.201501882>
- [31] Jiang J, Li Y, Liu J, Huang X, Yuan C, Lou XWD (2012) Recent advances in metal oxide-based electrode architecture design for electrochemical energy storage. *Adv Mater* 24:5166–5180. <https://doi.org/10.1002/adma.201202146>
- [32] Wang B, Chen JS, Wang Z, Madhavi S, Lou XWD (2012) Green synthesis of NiO nanobelts with exceptional pseudocapacitive properties. *Adv Energy Mater* 2:1188–1192. <https://doi.org/10.1002/aenm.201200008>
- [33] Sevilla M, Yu L, Zhao L, Ania CO, Titiric M-M (2014) Surface modification of CNTs with N-doped carbon: an effective way of enhancing their performance in supercapacitors. *ACS Sustain Chem Eng* 2:1049–1055. <https://doi.org/10.1021/sc500069h>
- [34] Ryu I, Kim G, Park D, Yim S (2015) Ethanedithiol-treated manganese oxide nanoparticles for rapidly responsive and transparent supercapacitors. *J Power Sources* 297:98–104. <https://doi.org/10.1016/j.jpowsour.2015.07.072>
- [35] Zhang LL, Zhao XS (2009) Carbon-based materials as supercapacitor electrodes. *Chem Soc Rev* 38:2520–2531. <https://doi.org/10.1039/b813846j>
- [36] Pendashteh A, Rahmanifar MS, Kaner RB, Mousavi MF (2014) Facile synthesis of nanostructured CuCo_2O_4 as a novel electrode material for high-rate supercapacitors. *Chem Commun* 50:1972–1975. <https://doi.org/10.1039/c3cc48773c>
- [37] Wang L, Lu X, Lei S, Song Y (2014) Graphene-based polyaniline nanocomposites: preparation, properties and applications. *J Mater Chem A* 2:4491–4509. <https://doi.org/10.1039/c3ta13462h>
- [38] Mondal S, Rana U, Malik S (2015) Graphene quantum dot-doped polyaniline nanofiber as high performance supercapacitor electrode materials. *Chem Commun* 51:12365–12368. <https://doi.org/10.1039/c5cc03981a>
- [39] Su C-I, Wang C-M, Lu K-W, Shih W-C (2014) Evaluation of activated carbon fiber applied in supercapacitor electrodes. *Fibers Polym* 15:1708–1714. <https://doi.org/10.1007/s12221-014-1708-4>
- [40] Chang W-M, Wang C-C, Chen C-Y (2015) Plasma treatment of carbon nanotubes applied to improve the high performance of carbon nanofiber supercapacitors. *Electrochim Acta* 186:530–541. <https://doi.org/10.1016/j.electacta.2015.11.038>
- [41] Moysowicz A, Śliwak A, Gryglewicz G (2015) Influence of structural and textural parameters of carbon nanofibers on their capacitive behavior. *J Mater Sci* 51:3431–3439. <https://doi.org/10.1007/s10853-015-9660-2>
- [42] Sun X, He J, Li G et al (2013) Laminated magnetic graphene with enhanced electromagnetic wave absorption properties. *J. Mater. Chem. C* 1:765–777. <https://doi.org/10.1039/c2tc00159d>
- [43] Zheng J, Lv H, Lin X, Ji G, Li X, Du Y (2014) Enhanced microwave electromagnetic properties of Fe_3O_4 /graphene nanosheet composites. *J Alloys Compd* 589:174–181. <https://doi.org/10.1016/j.jallcom.2013.11.114>
- [44] Nithya VD, Sabari Arul N (2016) Progress and development of Fe_3O_4 electrodes for supercapacitors. *J Mater Chem A* 4:10767–10778. <https://doi.org/10.1039/c6ta02582j>
- [45] Sun S, Zhai T, Liang C, Savilov SV, Xia H (2018) Boosted crystalline/amorphous Fe_2O_3 - δ core/shell heterostructure for flexible solid-state pseudocapacitors in large scale. *Nano Energy* 45:390–397. <https://doi.org/10.1016/j.nanoen.2018.01.015>
- [46] Li Y, Xu J, Feng T, Yao Q, Xie J, Xia H (2017) Fe_2O_3 nanoneedles on ultrafine nickel nanotube arrays as efficient anode for high-performance asymmetric supercapacitors. *Adv Funct Mater* 27:1606728. <https://doi.org/10.1002/adfm.201606728>
- [47] Zhou Y, Qin Z-Y, Li L et al (2010) Polyaniline/multi-walled carbon nanotube composites with core-shell structures as supercapacitor electrode materials. *Electrochim Acta* 55:3904–3908. <https://doi.org/10.1016/j.electacta.2010.02.022>
- [48] Qiu H, Han X, Qiu F, Yang J (2016) Facile route to covalently-jointed graphene/polyaniline composite and its enhanced electrochemical performances for supercapacitors. *Appl Surf Sci* 376:261–268. <https://doi.org/10.1016/j.apsusc.2016.03.018>
- [49] Rana U, Malik S (2012) Graphene oxide/polyaniline nanostructures: transformation of 2D sheet to 1D nanotube and in situ reduction. *Chem Commun* 48:10862–10864. <https://doi.org/10.1039/c2cc36052g>

- [50] Wang K, Wu H, Meng Y, Wei Z (2014) Conducting polymer nanowire arrays for high performance supercapacitors. *Small* 10:14–31. <https://doi.org/10.1002/sml.201301991>
- [51] Rana U, Chakrabarti K, Malik S (2012) Benzene tetracarboxylic acid doped polyaniline nanostructures: morphological, spectroscopic and electrical characterization. *J Mater Chem* 22:15665–15671. <https://doi.org/10.1039/c2jm33093h>
- [52] Qu B, Zhu C, Li C, Zhang X, Chen Y (2016) Coupling hollow Fe₃O₄-Fe nanoparticles with graphene sheets for high-performance electromagnetic wave absorbing material. *ACS Appl Mater Interfaces* 8:3730–3735. <https://doi.org/10.1021/acsami.5b12789>
- [53] Li L, Dou Y, Wang L, Luo M, Liang J (2014) One-step synthesis of high-quality N-doped graphene/Fe₃O₄ hybrid nanocomposite and its improved supercapacitor performances. *RSC Adv.* 4:25658–25665. <https://doi.org/10.1039/c4ra02962c>
- [54] Li H, Liao J, Xibin Z (2014) Facile synthesis of single crystal Fe₃O₄ sub-microcubes free of any capping agent and their catalytic performance in p-nitrophenol reduction. *J Mater Chem A* 2:17530–17535. <https://doi.org/10.1039/c4ta02966f>
- [55] Li X-G, Li A, Huang M-R (2008) Facile high-yield synthesis of polyaniline nanosticks with intrinsic stability and electrical conductivity. *Chem Eur J* 14:10309–10317. <https://doi.org/10.1002/chem.200801025>
- [56] Kuila T, Mishra AK, Khanra P, Kim NH, Uddin ME, Lee JH (2012) Facile method for the preparation of water dispersible graphene using sulfonated poly(ether-ether-ketone) and its application as energy storage materials. *Langmuir* 28:9825–9833. <https://doi.org/10.1021/la301469u>
- [57] Li Y, Zhao X, Yu P, Zhang Q (2012) Oriented arrays of polyaniline nanorods grown on graphite nanosheets for an electrochemical supercapacitor. *Langmuir* 29:493–500. <https://doi.org/10.1021/la303632d>
- [58] Ji L, Zhou L, Bai X et al (2012) Facile synthesis of multiwall carbon nanotubes/iron oxides for removal of tetrabromobisphenol A and Pb(II). *J Mater Chem* 22:15853–15862. <https://doi.org/10.1039/c2jm32896h>
- [59] Zeng S, Chen H, Cai F, Kang Y, Chen M, Li Q (2015) Electrochemical fabrication of carbon nanotube/polyaniline hydrogel film for all-solid-state flexible supercapacitor with high areal capacitance. *J Mater Chem A* 3:23864–23870. <https://doi.org/10.1039/c5ta05937b>